

Cite this: *Chem. Sci.*, 2021, **12**, 2050

All publication charges for this article have been paid for by the Royal Society of Chemistry

Defect mitigation using *D*-penicillamine for efficient methylammonium-free perovskite solar cells with high operational stability†

Jianchao Yang,‡^{ab} Weijian Tang,‡^a Ruihan Yuan,^a Yu Chen,^a Jing Wang,^c Yihui Wu,^{*a} Wan-Jian Yin, Ningyi Yuan, Jianning Ding,^{*bd} and Wen-Hua Zhang

Trap-dominated non-radiative charge recombination is one of the key factors that limit the performance of perovskite solar cells (PSCs), which was widely studied in methylammonium (MA) containing PSCs. However, there is a need to elucidate the defect chemistry of thermally stable, MA-free, cesium/formamidinium (Cs/FA)-based perovskites. Herein, we show that *D*-penicillamine (PA), an edible antidote for treating heavy metal ions, not only effectively passivates the iodine vacancies (Pb^{2+} defects) through coordination with the $-SH$ and $-COOH$ groups in PA, but also finely tunes the crystallinity of Cs/FA-based perovskite film. Benefiting from these merits, a reduction of non-radiative recombination and an increase in photoluminescence lifetime have been achieved. As a result, the champion MA-free device exhibits an impressive power conversion efficiency (PCE) of 22.4%, an open-circuit voltage of 1.163 V, a notable fill factor of 82%, and excellent long-term operational stability. Moreover, the defect passivation strategy can be further extended to a mini module (substrate: $4 \times 4 \text{ cm}^2$, active area: 7.2 cm^2) as well as a wide-bandgap ($\sim 1.73 \text{ eV}$) Cs/FA perovskite system by delivering PCEs of 16.3% and 20.2%, respectively, demonstrating its universality in defect passivation for efficient PSCs.

Received 19th November 2020
Accepted 17th December 2020

DOI: 10.1039/d0sc06354a
rsc.li/chemical-science

Introduction

Lead halide perovskite materials have recently demonstrated great potential in solar cells.¹ The highest laboratory power conversion efficiencies (PCEs) of perovskite solar cells (PSCs) have been risen to over 25%.² To date, methylammonium (MA) containing perovskites are widely employed as light-absorbers for the majority of the highly efficient PSCs.^{1d,3} However, the presence of MA is considered to be one of the main factors that limit the long-term stability of PSCs, because $MAPbI_3$ is thermally unstable and decomposes at elevated temperature (e.g., $\sim 85^\circ\text{C}$).⁴ Alternatively, a formamidinium (FA) based perovskite

was employed to counter these issues due to its improved thermal stability (up to 150°C) along with its favorable optical bandgap (1.48 eV) for absorbing solar irradiation.⁵ However, other ions, such as MA^+ ,^{1d} Cs^+ (Rb^+),⁴ as well as low-dimensional perovskites,⁶ are still required to stabilize the photoactive black α - $FAPbI_3$.⁷ The development of MA-free (where it refers to not only the resultant perovskite film, but also the precursor solution), Cs/FA perovskites is potentially an effective strategy to address the intrinsic thermal instability related to perovskite materials.⁸ Benefiting from their excellent thermal and optoelectronic properties, the Cs/FA based PSCs have recently gained increasing attention.⁹ A variety of approaches, such as heterojunction engineering,^{9c,10} interfacial modification^{9a,11} and crystallization tailoring^{9b} have been carried out to improve the device performance. The highest efficiency of 22.2% has been most recently reported by constructing a graded two-dimensional/three-dimensional (2D/3D) perovskite heterostructure for the Cs/FA-based PSCs (the recent progress in MA-free, Cs/FA-based PSCs with normal structures is summarized in Table S1, ESI†).^{9c} Nevertheless, compared to the highly efficient MA-containing perovskite device, it is still necessary to deeply understand the fundamental physicochemical properties and to further elevate the performance of Cs/FA-based PSCs.

The defect chemistry of perovskites is an important issue in affecting the performance of PSCs.¹² Defects in the perovskite films are reported to be charged due to their ionic nature.¹³ In particular, point defects such as halide anion vacancies and

^aSichuan Research Center of New Materials, Institute of Chemical Materials, China Academy of Engineering Physics, 596 Yinhe Road, Shuangliu, Chengdu 610200, China. E-mail: yihuiwu@caep.cn; whzhang@caep.cn

^bJiangsu Collaborative Innovation Center of Photovoltaic Science and Engineering, Changzhou University, Changzhou, 213164, China. E-mail: dingjn@cczu.edu.cn

^cCollege of Energy, Soochow Institute for Energy and Materials InnovationS (SIEMIS), Soochow University, Suzhou, 215006, China. E-mail: wjyin@suda.edu.cn

^dMicro/Nano Science and Technology Center, Jiangsu University, Zhenjiang 212013, China

† Electronic supplementary information (ESI) available: Detailed experimental parts, FTIR spectrum, XPS spectrum, theoretical calculation results, XRD, SEM images, AFM, UV-vis absorption spectra, UPS spectra, statistics of device performance, hysteresis behavior of the devices, steady I-T, SCLC, and tables that summarize the TRPL, EIS and *J-V* parameters. See DOI: [10.1039/d0sc06354a](https://doi.org/10.1039/d0sc06354a)

‡ These authors contributed equally to this work.



organic cation vacancies are easily formed in perovskite materials because of their low formation energies. These electronic traps are distributed at the surface and grain boundaries, or in the bulk of the perovskite films, thereby providing additional energy levels that act as recombination centers in the perovskites. Electronic traps are the origin of non-radiative recombination that tend to limit the open-circuit voltage (V_{OC}),^{4,5,14} and also cause rapid decomposition of the perovskite absorber; this is because they present an initiation site for degradation by extrinsic environmental species.^{13a} Therefore, passivating the charged defects in perovskites using electrostatic interactions or chemical interactions can suppress charge-carrier recombination and is vitally important for high-performance PSCs. Tremendous efforts have been devoted to control and mitigate defects in perovskites.^{12,13} For example, introducing excess MA/FA or iodine ions to the precursor has been demonstrated to be an effective method for suppressing organic cation or halide anion vacancies.¹⁵ The ionic nature of perovskites also enables defect passivation based on Lewis acid-base chemistry using functional molecules containing carbonyl, sulfonic acid, and quaternary ammonium groups.¹⁶ Huang *et al.* employed choline chloride to passivate both the negative and the positive charged defects by quaternary ammonium and halide ions, respectively.¹² A simultaneous passivation of anion and cation vacancies can also be achieved by fluoride, attributable to the extremely high electronegativity of fluoride by forming hydrogen bond with $-\text{NH}_3$ and ionic bond with Pb^{2+} .^{13a} However, most of these studies have focused on defect passivation in MA-containing high-efficiency perovskite systems, and research on the defect chemistry in thermally stable, MA-free, Cs/FA-based perovskites has rarely been reported.

Herein, an edible antidote, α -penicillamine (PA) with triple functional groups (thiol ($-\text{SH}$), carboxylic ($-\text{COOH}$), and amine ($-\text{NH}_2$)), is introduced to passivate the charged traps in an MA-free, Cs/FA double-cation lead halide perovskite film (with the composition of $\text{Cs}_{0.15}\text{FA}_{0.85}\text{Pb}(\text{I}_{0.95}\text{Br}_{0.017}\text{Cl}_{0.033})_3$). PA is a strong chelating agent and has been widely adopted in treating heavy metal toxicity in medicine, because it is safe for humans and can react with the majority of heavy metal ions, particularly those with an affinity for sulfur.¹⁷ Therefore, on one hand, the incorporation of PA effectively immobilizes the uncoordinated Pb^{2+} (iodine vacancy) by coordination with $-\text{SH}$ and/or $-\text{COOH}$ functional groups, which hence suppress the formation of metallic Pb defects and reduce non-radiative recombination. On the other hand, the crystallinity of the perovskite film is also improved, and a considerably increased photoluminescence lifetime is observed. Benefiting from these merits, a V_{OC} of 1.163 V (with V_{OC} loss of only 0.4 V) and a fill factor (FF) of 82% are ultimately obtained for the n-i-p structured planar PSCs, which is superior to those of the control device ($V_{OC} = 1.116$ V, FF = 78%). The champion device gives a PCE of 22.4%, a very impressive efficiency for the MA-free, Cs/FA based PSCs reported to date. Meanwhile, the PA passivated device exhibits excellent long-term stability, retaining more than 95%, 88%, and 82% of the initial efficiencies after one year of storage in the dark, 260 h of maximum output power point tracking under ~ 1 sun illumination, and 1200 h of thermal aging at 85 °C,

respectively. A mini module with an active area of 7.2 cm² is also fabricated on a 4 × 4 cm² substrate, delivering a PCE of 16.3%. The present strategy can be further extended to wide-bandgap PSCs, and an efficiency of 20.2% has been achieved for Cs/FA-based PSCs ($E_g = 1.73$ eV), demonstrating the universality of the present defect passivation strategy.

Results and discussion

To study the influence of PA on the defects of perovskites, we introduced a trace amount of PA molecules (0.01 mg mL⁻¹) to the Cs/FA-based perovskite precursor solution. The perovskite thin film is fabricated using a green anti-solvent processed spin-coating method.¹⁸ The interaction between PA and lead ions in the perovskite can be revealed by Fourier transform infrared (FTIR) spectroscopy. Fig. S1, ESI† shows the FTIR spectra for PA, perovskite and PA passivated perovskite samples. Three characteristic functional groups were detected for PA alone and PA-containing perovskites, namely: $-\text{SH}$, $-\text{COOH}$, and $-\text{NH}_2$,¹⁹ this indicated the successful incorporation of PA in the perovskite film. For the PA passivated perovskite sample, the peaks for $-\text{SH}$ (~ 2519 cm⁻¹, ~ 2613 cm⁻¹) and $-\text{COOH}$ (~ 1600 cm⁻¹, ~ 1400 cm⁻¹) functional groups shifted to lower wavenumbers in comparison with the neat PA (Fig. 1a).^{19,20} This is attributed to the interaction between PA and Pb^{2+} , where $-\text{C}=\text{O}$ and $-\text{SH}$ may synergistically donate their unpaired lone electron to the empty orbitals of Pb^{2+} . A similar case occurs in the DMSO/perovskite system where the sulfonic group ($-\text{S}=\text{O}$) of the DMSO molecule can strongly interact with Pb^{2+} .²¹ Liquid-state ¹H nuclear magnetic resonance (NMR) spectroscopy was performed to further evaluate the interaction between PA and PbI_2 . Fig. 1b shows that a shift in the proton signal occurs for the PbI_2 -PA solution in contrast to neat PA, particularly for the proton at the α -site of the carboxyl group. This further confirms the existence of a strong coordinating interaction between Pb^{2+} and $-\text{C}=\text{O}$ and $-\text{SH}$ functional groups in PA.²² A similar conclusion can again be reached from UV-Vis absorption spectra. As shown in Fig. 1c, a significant red shift of the absorption spectra and a change in the color of the solution were observed for the PA- PbI_2 mixed solution compared to the pure PA and PbI_2 solutions, indicative of the interaction between PbI_2 and the functional groups in PA. Fig. S2, ESI† shows the X-ray photoelectron spectroscopy (XPS) results for the perovskite films with and without PA (to vividly observe the presence of sulfur, 1 mg mL⁻¹ PA was used). The characteristic peaks for S^{2-} at approximately 164 eV (Fig. 1d) verified the presence of PA in the target film. The peaks at 142.6 and 137.7 eV were assigned to Pb^{2+} , while the two shoulders at 140.9 and 136.0 eV were ascribed to metallic Pb (Pb^0), resulting from uncoordinated Pb^{2+} defects (iodine vacancy) produced during the thermal annealing process (Fig. 1e). Those defects are identified as recombination centers that can lead to a deterioration of the photovoltaic (PV) performance of PSCs.²³ The intensity ratio of $\text{Pb}^0/(\text{Pb}^0 + \text{Pb}^{2+})$ was found to be 5.2% for the control sample. However, the intensity ratio significantly reduced to 2.2% after introducing the PA functional molecule, indicating that this molecule can effectively suppress the formation of Pb^0 defects.²³ Additionally,



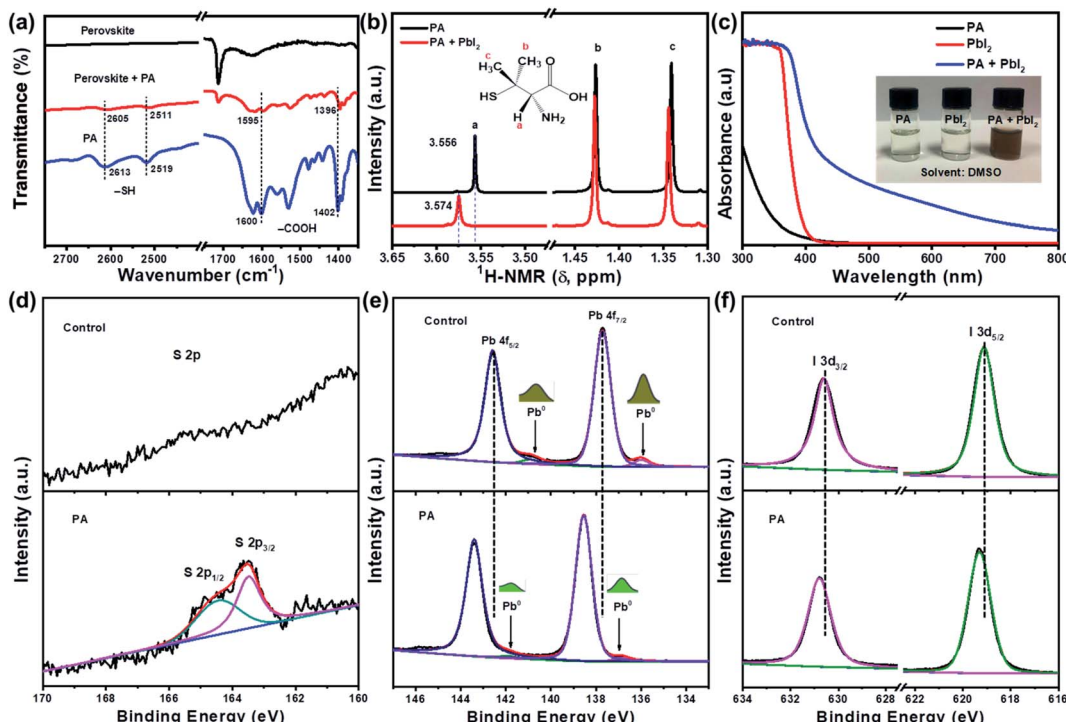


Fig. 1 (a) FTIR spectra of PA and perovskite films without and with PA. (b) ^1H -NMR spectra of PA and PA containing PbI_2 solutions. (c) UV-vis absorption spectra of PbI_2 solutions without and with PA (inset: photographs of the corresponding solution). High resolution XPS spectra of S 2p (d), Pb 4f (e) and I 3d (f) for the perovskite films without and with PA, respectively.

the characteristic peaks of Pb^{2+} shifted to a higher binding energy after the introduction of PA, which could be ascribed to the increased interaction between the perovskite and PA through a coordination reaction.²⁴ A similar phenomenon was observed for the I 3d peaks (Fig. 1f), attributable to the electrostatic interaction between I (iodine) and $-\text{NH}_2$ groups in PA by hydrogen bonding.^{16b,25}

To confirm the passivation mechanism of PA within the perovskite, density functional theory (DFT) calculations were employed.²⁶ The band structure and projected density of states (PDOS) for a perfect perovskite structure are shown in Fig. S3, ESI.† It can be found that the valence band maximum (VBM) and the conduction band minimum (CBM) of the perovskite are mainly composed of iodine orbitals and lead orbitals, respectively, while the A-site cations make negligible contribution on the band edges. When an iodine vacancy (V_I) and an A-site cation vacancy (such as V_{Cs}) are simultaneously introduced on the outermost surface (Fig. S3, ESI†), no defect states were created in the corresponding system. However, when two adjacent V_I are introduced simultaneously on the outermost surface (Fig. 2a and b), the lattice structure near the defects significantly changed, forming a Pb–Pb dimer (3.35 \AA). This dimer configuration results in the formation of a relatively deep, doubly occupied defect state below the CBM (0.68 eV). Fortunately, when the PA molecule was introduced (Fig. 2c and d), it not only effectively suppresses the formation of the Pb–Pb dimer, but also saturates the dangling bonds of Pb at the surface by coordination with the O and S groups in PA, resulting

in the elimination of the deep-level defect state. These results indicate that the strong interactions between the perovskite and PA molecule can effectively passivate vacancy defects (V_I) within the perovskite, which is beneficial for improving device performance.

To gain insight into the influence of PA molecules on the crystallinity of the perovskite, the as-prepared perovskite films with and without PA were subsequently investigated using X-ray

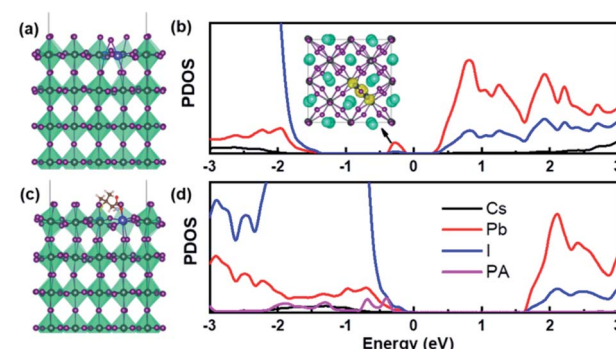


Fig. 2 Optimized geometry (a and c) and projected density of states (b and d) of the surface (001) with two adjacent iodine vacancies and the same surface with an adsorbed PA molecule, respectively. For better visualization, we remove the A-site cations of corresponding structures, because the contributions of these cations in the band edge are negligible. The under-coordinated Pb atoms are highlighted by the blue solid balls. The inset (b) shows the charge density of the trap state caused by the Pb–Pb dimer.



diffraction (XRD). All perovskite films, containing different amounts of PA, exhibited the same crystal structure and hexagonal non-perovskite phases were not detected (Fig. S4a, ESI†), indicative of the formation of a phase-pure photoactive perovskite. With increase in the PA concentrations, the intensity of the diffraction peak at the (110) plane gradually increased and showed a maximum for the sample containing 0.01 mg mL^{-1} PA (Fig. 3a and b). In the meantime, its corresponding full width at half maximum gradually decreased and exhibited a minimum for the perovskite film with 0.01 mg mL^{-1} PA (Fig. S4b, ESI†). These were attributed to an improvement in the crystallinity of perovskite with the addition of PA. Moreover, the intensity ratio of the diffraction peaks at (110)/(112) (located at 14.11° and 20.06° , respectively) also increased from 1.70 for the control film to 2.98 for the 0.01 mg mL^{-1} PA-passivated perovskite film (Fig. 3b), demonstrating that the crystal growth direction was preferred along the (110) facet. The (110) orientation of the perovskite film is conducive to hole transfer from the perovskite to HTMs, owing to the increased electrostatic potential and enhanced electronic cloud overlapping at the interface.²⁷ These results suggest that the presence of PA in the precursor promoted the crystallization and orientation of the perovskite film. The surface morphologies of the perovskite films with and without 0.01 mg mL^{-1} PA were studied by scanning electron microscopy (SEM). Fig. 3c and S5, ESI† show that the control sample is fully covered by polycrystalline perovskite and the average crystal size of the perovskite is approximately 210 nm (Fig. S5, ESI†). After the introduction of PA, the average crystal size is increased to 292 nm (Fig. 3d), indicating that the crystal quality of the perovskite film was improved, in good agreement with the XRD results. The root-

mean-square (RMS) roughness was measured using atomic force microscopy (AFM). The RMS decreased from 23.3 nm for the control film to 17.7 nm for the film containing PA (Fig. S6, ESI†). A smoother surface usually indicates a higher quality film in PSCs. In addition, all perovskite films with and without PA exhibit a bandgap of $\sim 1.56 \text{ eV}$ and no significant changes in the absorption intensity were observed with variation in PA concentration (Fig. S7, ESI†), suggesting that the presence of PA doesn't influence the intrinsic optical properties of the perovskite. The band tail width (Urbach energy, E_u) was reported to depend on the charged defects at both the grain boundaries and the surface in perovskites and it can be calculated from the UV-Vis absorption spectra.²⁸ As shown in Fig. 3e, the E_u values for the pristine and PA-passivated perovskite films were estimated to be 24.4 and 18.9 meV, respectively. The decrease in the E_u is indicative of the reduced disorder of shallow energy levels and the increased electronic quality of the perovskite film as a result of passivated charged defects.²⁹

Steady state photoluminescence (PL) and time-resolved PL (TRPL) spectroscopies were employed to evaluate the charge-carrier dynamics in the perovskite films. The perovskite film containing PA exhibited stronger PL intensity than the control film (Fig. 3f), demonstrating that the quality of the perovskite film was significantly improved with the addition of PA. TRPL results (Fig. 3g) further confirm this conclusion. The TRPL decay curves were fitted with a bi-exponential function (eqn (1)) and the fitted data are summarized in Table S2, ESI†

$$f(t) = A_1 \exp\left(-\frac{t}{\tau_1}\right) + A_2 \exp\left(-\frac{t}{\tau_2}\right) + B \quad (1)$$

where τ_1 is the fast decay process related to bimolecular recombination, and τ_2 is the slow decay process associated with

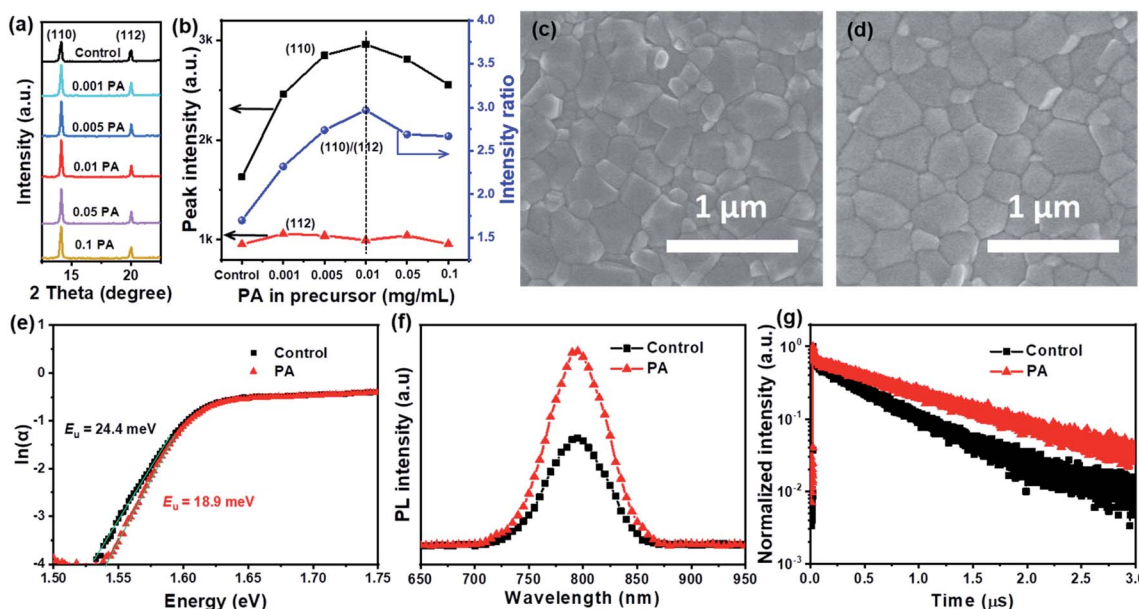


Fig. 3 (a) Partially enlarged XRD patterns of the perovskite films with different PA concentrations in the precursor. (b) Intensity of diffraction peaks at the (110), (112) planes and corresponding ratios derived from (a). SEM images of perovskite films without (c) and with 0.01 mg mL^{-1} PA (d) in the precursor solutions. (e) E_u values for the control and 0.01 mg mL^{-1} PA containing perovskite films. (f) PL and TRPL of the perovskite films without and with 0.01 mg mL^{-1} PA.



trap-assisted recombination.¹² B is a constant for the baseline offset. A_1 and A_2 are constants representing the contributions of the fast and slow components, respectively.³⁰ Notably, the PA molecule primarily impacted the slow decay process and the recombination time increased from 544.4 ns to 905.9 ns after introducing PA (Table S2, ESI†), suggesting that PA can effectively passivate the trap-states in perovskite. The average PL decay lifetime can be obtained using eqn (2):

$$\tau_{\text{ave}} = \frac{\sum A_i \tau_i^2}{\sum A_i \tau_i} \quad (2)$$

The average PL lifetime (τ_{ave}) for the control perovskite film was calculated to be 537 ns and was enhanced to 901 ns for the PA-passivated perovskite film, revealing the significantly improved film quality.¹² Improved PL lifetime correlates with reduced non-radiative recombination, which is strongly related to the V_{OC} . Therefore, a higher V_{OC} can be expected for the PA-passivated perovskite device.

Planar normal structured perovskite devices with a simple architecture (inset of Fig. 4a) consisting of FTO/c-TiO₂/perovskite/spiro-OMeTAD/Au were fabricated to evaluate the impact of the PA passivator on the photovoltaic (PV) performance, where FTO is fluorine-doped tin oxide, spiro-OMeTAD is 2,2',7,7'-tetrakis(*N,N*-dimethoxyphenylamine)-9,9'-spirobifluorene. The corresponding thicknesses of the compact TiO₂, perovskite layer and hole transporting layer (HTL) for a typical device were determined to be ~40 nm, ~600 nm and ~270 nm from the cross-sectional SEM images (Fig. S8, ESI†), respectively. The energy levels of the perovskite films with and without PA were measured using ultraviolet photoelectron spectroscopy

(UPS) (Fig. S9, ESI†). The CBMs of the perovskites slightly shifted from -3.92 eV to -3.94 eV after PA treatment (inset of Fig. 4a). Moreover, ΔE , denoting the difference between the Fermi-level and the CBM of the perovskite, gradually decreased from 0.28 to 0.21 eV for the perovskites without and with PA, respectively, indicative of the increased n-type behavior of the PA-perovskite.³¹ The downshifted energy levels and the reduced ΔE are beneficial for electron transfer. Fig. S10, ESI† shows the statistical device performance with different PA concentrations. As the concentration of PA increased, the average PCE of 40 individual devices increased from 20.2% for the control device to 21.8% for the device containing 0.01 mg mL⁻¹ PA. A further increase in the concentration of PA resulted in lower device efficiency. The decrease in the device performance was mainly reflected in the V_{OC} and FF (Fig. S10, ESI†), which should be ascribed to the changes in the crystal quality of perovskite films. These results are in good agreement with the XRD results (Fig. 3a and b), suggesting that the preferred crystal orientation and improved crystallinity of perovskite film with PA treatment could benefit the charge transportation and device performance.

Fig. 4a presents the J - V characteristics of the champion devices with and without PA under standard AM 1.5 illumination (at 100 mW cm⁻²). The main PV parameters, including the short circuit current density (J_{SC}), V_{OC} , FF, and PCE, are summarized in Table 1. A PCE of 20.7%, $J_{\text{SC}} = 23.72$ mA cm⁻², $V_{\text{OC}} = 1.116$ V, and FF = 78.17%, were obtained for the control device. Notably, the optimized PA-passivated device delivered a highly impressive PCE of 22.4%, with $J_{\text{SC}} = 23.52$ mA cm⁻², $V_{\text{OC}} = 1.163$ V, and FF = 81.97%. Besides, the hysteretic index (HI, defined as $(\text{PCE}_{\text{Re}} - \text{PCE}_{\text{Fw}})/\text{PCE}_{\text{Re}}$) is reduced from 7.7% for

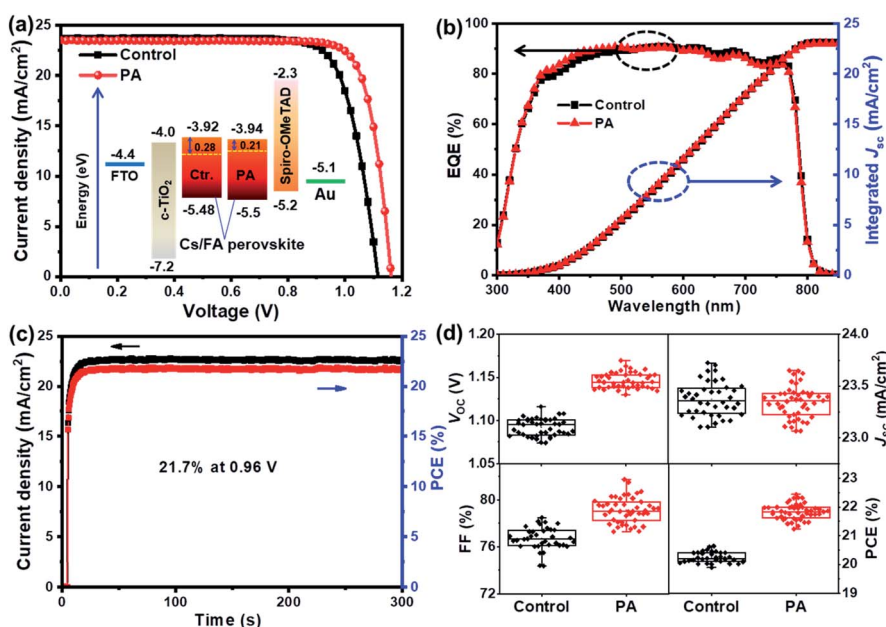


Fig. 4 (a) J - V curves of the champion devices based on the control and PA containing perovskite (inset: the device structure and the corresponding energy level alignment). (b) EQE curves and the corresponding integrated photocurrent for both devices. (c) Stabilized output efficiency of the device based on the PA containing perovskite around the maximum output power point as a function of time under simulated 1 sun illumination. (d) Statistics of PV parameters (J_{SC} , V_{OC} , FF, and PCE) for the devices based on the control and PA containing perovskites.



Table 1 The key photovoltaic parameters of the PSCs without and with PA

Perovskites	Scan direction	V_{OC} (V)	J_{SC} (mA cm $^{-2}$)	FF (%)	PCE (%)	HI (%)
Control	Reverse	1.116	23.72	78.17	20.7	7.7
	Forward	1.072	23.70	75.25	19.1	
With PA	Reverse	1.163	23.54	81.97	22.4	5.8
	Forward	1.139	23.52	78.78	21.1	

the control sample to 5.8% for the PA-passivated device (Fig. S11, ESI† and Table 1). Considering that the bandgap of the perovskite employed in this study was ~ 1.56 eV (Fig. S7, ESI†), the V_{OC} deficit for the champion device was only 0.40 V, which was comparable to the values observed in silicon solar cells (0.38 V);³² this result indicated one of the lowest reported values for MA-free PSCs.

The integrated photocurrent densities obtained from the external quantum efficiency (EQE) spectra were calculated to be 23.15 and 23.03 mA cm $^{-2}$ for the control and PA-passivated devices, respectively (Fig. 4b), both of which are comparable to the values extracted from the J – V curves. To accurately evaluate the real output performance of the devices, the steady-state output efficiency was measured around the maximum power point voltage (V_{mpp}). As shown in Fig. 4c and S12, ESI† the PA-passivated device stabilized at 21.7% ($V_{mpp} = 0.96$ V), whereas the control device yielded an output efficiency of 20.1% ($V_{mpp} = 0.92$ V). These results demonstrate the advantages of PA passivation in achieving PSCs with both high efficiency and super high V_{OC} . To confirm the reliability of our method, 40 individual cells for the control and passivated devices were fabricated and the detailed parameters (V_{OC} , J_{SC} , FF, and PCE) are displayed in Fig. 4d. Evidently, all the key parameters of the PA-passivated device show similar values with minor deviations, confirming the excellent batch-to-batch reproducibility.

To understand the improvement in the PV performance, the space-charge-limited current (SCLC) method was employed to examine the defect states in the perovskite layer with and without PA. The trap density, n_t , can be determined using eqn (3).³³

$$V_{TFL} = \frac{en_t L^2}{2\epsilon\epsilon_0} \quad (3)$$

where V_{TFL} is the trap-filled limit voltage, n_t is the trap density, L is the thickness of perovskite film, ϵ is the relative dielectric constant of the perovskite, and ϵ_0 is the vacuum permittivity. Fig. 5a shows the corresponding current–voltage (I – V) curves measured for electron-only and hole-injecting devices (Fig. S13, ESI†), respectively. The density of electron traps decreased from 2.75×10^{15} cm $^{-3}$ for the control sample to 1.52×10^{15} cm $^{-3}$ for the PA passivated device. Correspondingly, the density of hole traps was reduced from 6.61×10^{14} cm $^{-3}$ for the control device to 4.64×10^{14} cm $^{-3}$ for the latter one (Fig. S13, ESI†). The significantly reduced trap density should be attributed to the improved crystallinity, agreeing well with the TRPL results. The V_{OC} of a solar cell is reported to be strongly related to trap-assisted (non-radiative) recombination in the bulk and on the surface of the absorber layer.³⁴ The higher V_{OC} (1.163 V) for the PA passivated PSCs should be attributed to the decreased trap states subject to the PA modification.

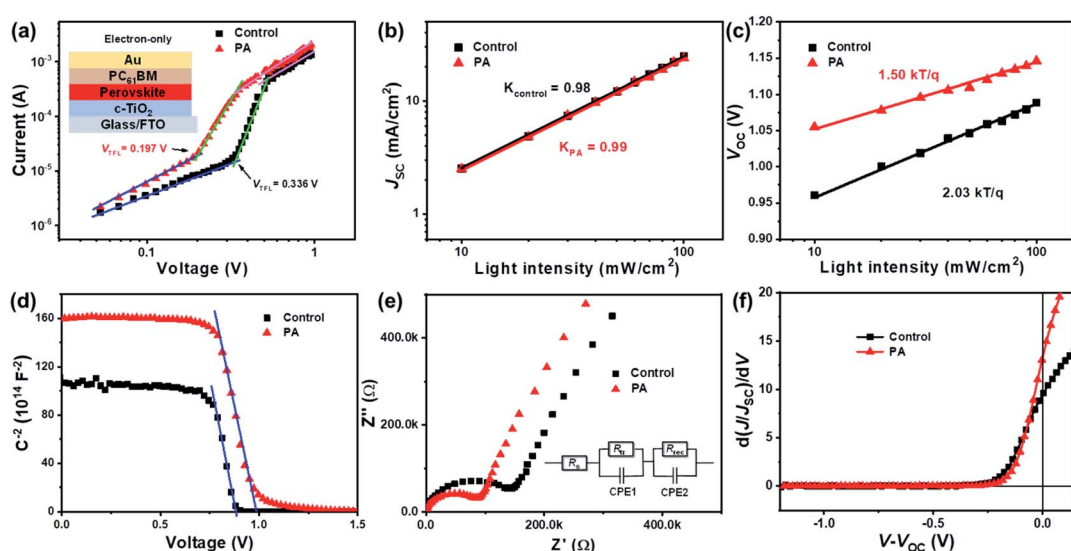


Fig. 5 (a) Dark I – V curves for the electron-only devices based on the control and PA containing perovskite. (b) J_{SC} vs. light intensity and (c) V_{OC} vs. light intensity for the devices without and with PA. (d) Mott–Schottky fitting to the capacitance–voltage (C^{-2} – V) plots and (e) EIS of PSCs based on control and PA containing perovskite film. (f) The slopes of the normalized J – V curves at each voltage for the champion control and PA containing devices.



To further understand the recombination mechanism in the devices, the J - V curves under different light intensities were studied for both devices. Fig. 5b shows the power-law dependence of J_{SC} on the incident light intensity (0.1 sun \leq light intensity ≤ 1 sun). For a solar cell with no space charge effect, the slope of the fitted line should be close to unity because of the small difference between the mobility of holes and electrons. The control device displays a slope of 0.98, while the PA containing device presents a slope of 0.99, indicating that the space charge effect is negligible for both devices and the predominant recombination mechanism is trap-assisted recombination.³⁵ Fig. 5c shows the relationship between light intensity and V_{OC} .³⁶ The deviation of the ideality factor (n) from unity is reported to be caused by non-radiative recombination in solar cells. The value of n was calculated to be 2.03 for the control device, and reduced to 1.50 for the PA-containing device. These results indicate that the trap-assisted non-radiative recombination process was effectively suppressed by PA molecules,³⁷ in good agreement with the results of the SCLC method. To better understand the enhancement of the V_{OC} , Mott–Schottky (M–S) analysis was performed (Fig. 5d).^{3a} The built-in potential (V_{bi}) can be extracted from the capacitance–voltage (C^{-2} – V) plots. The V_{bi} for the control device was

determined to be 0.88 V, increasing to 0.99 V for the PA-passivated device. The significantly improved V_{bi} implies an enhanced driving force for the separation of photogenerated carriers, which is favorable for achieving a higher V_{OC} . Therefore the increase in V_{bi} is another reason for the improvement of the V_{OC} .

Electrochemical impedance spectroscopy (EIS) was employed to study the interfacial carrier transfer and transport kinetics. Fig. 5e shows the Nyquist plots of the control and PA-passivated devices at 0 V applied bias voltages in the dark. The Nyquist plots can be divided into two different parts: the arcs present in the high-frequency region are related to the charge-transport resistance (R_{tr}) and the incomplete semicircles present in the low frequency region represent the recombination resistance (R_{rec}) of PSCs.³⁷ The corresponding values of R_{tr} and R_{rec} were fitted using the Z-view software with the given equivalent circuit (Fig. 5e) and are summarized in Table S3, ESI.† A lower R_{tr} and a higher R_{rec} were obtained for the device containing PA compared with the control one, indicative of a faster charge-carrier transfer and a lower recombination rate for the PA-passivated device, in good agreement with the aforementioned characterization results. The impact of PA molecules on the charge collection within the cells can be

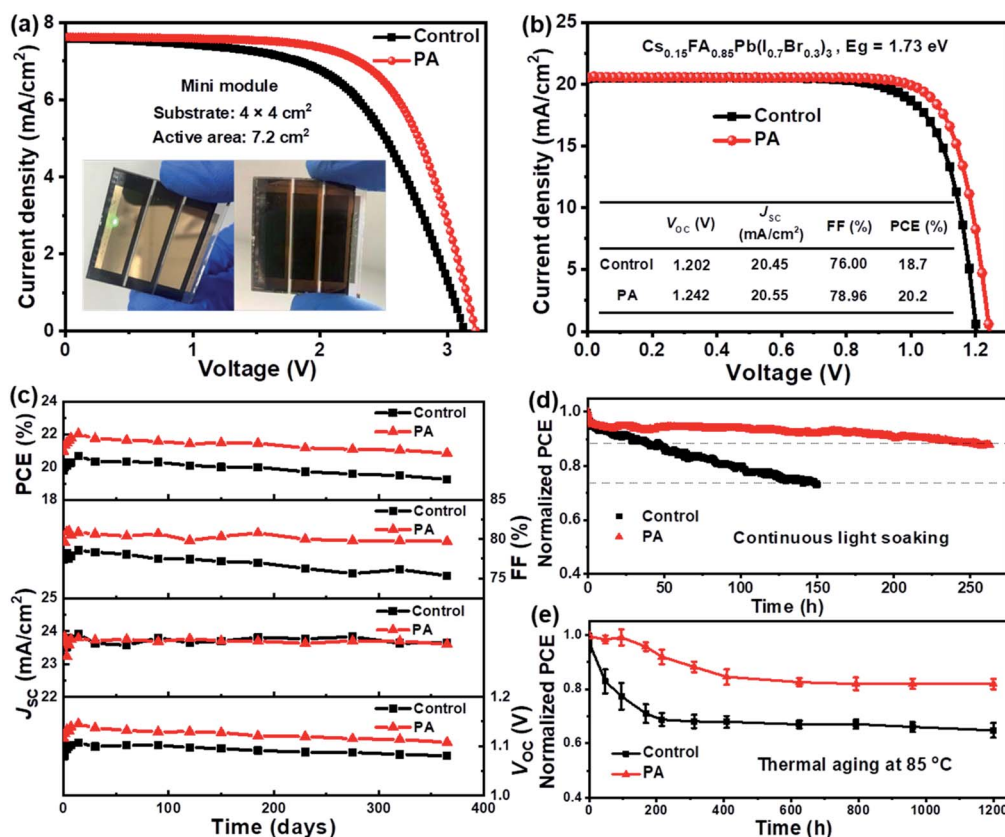


Fig. 6 (a) J - V curves of the mini perovskite solar modules (inset: photographs of the mini modules) and (b) the wide-bandgap Cs/FA-based PSCs based on the control and PA containing perovskite. (c) Long-term stability of the unsealed devices based on the control and PA containing perovskite stored in the dark under ambient air conditions with $\sim 35\%$ relative humidity. (d) Continuous light soaking of the control and PA containing PSCs at short circuit under ~ 1 sun illumination (white light LED) in a N_2 -filled glovebox, the data were automatically collected every 10 s. (e) Normalized efficiencies of the control and PA containing PSCs under continuously heating at 85 °C in a N_2 -filled glove box.

experimentally verified from the normalized *J*-*V* curves (Fig. S14, ESI†). Fig. 5f shows the slope of the *J*-*V* curves as a function of the applied voltage.³⁸ The PA-passivated device exhibits a charge collection efficiency of 13.2 at open circuit, which is higher than that of the control one (11.5). These results indicate that highly efficient charge collection can be expected for the PA containing device, leading to higher V_{OC} and FF values.^{38a} In other words, the improvement in the PV performance of the passivated device is attributed to the improved crystallinity, increased charge transfer, enhanced collection efficiency, and reduced non-radiative recombination.

To assess the large-area compatibility and effectiveness of our strategy on the laboratory scale, a mini perovskite solar module was fabricated on a $4 \times 4 \text{ cm}^2$ FTO substrate. As shown in Fig. 6a, each module contained three single cells connected in series with a total active area of 7.2 cm^2 (the detailed fabrication process and the module structure are shown in Fig. S15 and S16, ESI†). The control module, based on the pristine perovskite, presented a PCE of 13.9% with $J_{SC} = 7.59 \text{ mA cm}^{-2}$, $V_{OC} = 3.132 \text{ V}$, and FF = 58.41%. After the introduction of PA, a PCE of 16.3%, $J_{SC} = 7.63 \text{ mA cm}^{-2}$, $V_{OC} = 3.222 \text{ V}$, and FF = 66.19% were achieved for the optimized module. The improvement in the device efficiency is reflected in the V_{OC} and FF values, following the same trend with the small-area PSCs discussed above. To further verify its universality, the present defect passivation strategy was applied to a wide-bandgap perovskite. The control device, using $\text{Cs}_{0.15}\text{FA}_{0.85}\text{Pb}(\text{I}_{0.7}\text{Br}_{0.3})_3$ ($E_g = 1.73 \text{ eV}$) as the light absorber, delivered a PCE of 18.7% (Fig. 6b), whereas the PCE and V_{OC} significantly improved to 20.2% and 1.242 V, respectively, for the PA-passivated device. This value is among the highest efficiencies reported for hybrid wide-bandgap PSCs,^{29,39} thereby showing great promise for use as a top-cell in tandem solar cells.⁴⁰

Finally, we evaluated the stability of both devices under ambient air conditions at room temperature and 35% relative humidity. Fig. 6c and Table S4, ESI† show the main parameters for the control and PA-passivated devices without encapsulation. More than 95% of its original efficiency (22.02%) was obtained for the PA-passivated device after one year of storage, demonstrating the excellent ambient stability of the device. We subsequently investigated the operational stability of the unencapsulated devices. As shown in Fig. 6d, the PA containing device retained over 88% of its original efficiency after 260 h of continuous MPP tracking under ~ 1 sun illumination (white light LED, N_2 filled glovebox, $\sim 30^\circ\text{C}$), whereas the control device retains only 73% of its initial PCE after 150 h under identical conditions. To further evaluate the thermal stabilities of the devices, the unstable spiro-OMeTAD was replaced with PTAA [poly[bis(4-phenyl)(2,4,6-trimethylphenyl)amine]].^{1e,23,41} As shown in Fig. 6e, the PA-passivated device, without encapsulation, retained over 82% of its initial efficiency after 1200 h of thermal aging at 85°C (N_2 filled glovebox). These results demonstrate that the present Cs/FA-based PSCs with the PA passivator exhibited excellent long-term operational stability, and the improved stability of the PSCs is attributed to the improved crystal quality and reduced defects in the perovskite film after PA passivation.^{5,14}

Conclusions

In summary, we have developed a facile regulation strategy that simultaneously improves crystallinity and passivates the defects in Cs/FA perovskites, resulting in improved efficiencies and stabilities of the resultant PSCs. The formation of a deep-level defect state derived from the iodine vacancy defects was effectively suppressed as a result of the strong coordination between the functional groups ($-\text{SH}$ and $-\text{COOH}$) in the PA molecule and uncoordinated Pb^{2+} present in the perovskite. As such, non-radiative recombination within the perovskite film was significantly reduced. Furthermore, the crystallization process and crystal quality were improved because of the presence of PA. The improved crystallinity, with suppressed non-radiative recombination, led to a high V_{OC} of 1.163 V (with a voltage deficit of 0.4 V), a remarkable FF of 82%, and a champion PCE of 22.4% along with a steady-state output efficiency of 21.7%. Additionally, the unencapsulated devices containing PA exhibited excellent ambient, operational, and thermal stabilities. Finally, the present strategy was further extended to both a mini solar module ($4 \times 4 \text{ cm}^2$ substrate) and a wide-bandgap ($\sim 1.73 \text{ eV}$) perovskite system with impressive performance. Our findings demonstrate that rational defect mitigation is an effective method to produce highly stable and efficient PSCs.

Author contributions

Jianchao Yang: validation, formal analysis, investigation, resources, data curation. Weijian Tang: validation, formal analysis, investigation, resources, data curation. Ruihan Yuan: investigation, resources. Yu Chen: investigation, resources. Jing Wang: investigation, resources. Yihui Wu: conceptualization, methodology, writing-original draft, writing-review & editing, visualization, supervision, funding acquisition. Wan-Jian Yin: writing-review & editing, supervision. Ningyi Yuan: writing-review & editing. Jianning Ding: writing-review & editing, supervision. Wen-Hua Zhang: writing-review & editing, supervision, funding acquisition, project administration.

Conflicts of interest

There are no conflicts to declare.

Acknowledgements

The authors thank the support from the National Natural Science Foundation of China (Grant No. 61904166 and 21773218), Talents of Science and Technology Innovation in Sichuan province (Grant No. 2018RZ0119), Anshan Hifichem Co. Ltd, and the Jiangsu Province Cultivation base for State Key Laboratory of Photovoltaic Science and Technology.

Notes and references

- (a) A. Kojima, K. Teshima, Y. Shirai and T. Miyasaka, *J. Am. Chem. Soc.*, 2009, **131**, 6050; (b) B. Cai, Y. Xing, Z. Yang, W.-H. Zhang and J. Qiu, *Energy Environ. Sci.*, 2013, **6**, 1480;



(c) M. Z. Liu, M. B. Johnston and H. J. Snaith, *Nature*, 2013, **501**, 395; (d) Q. Jiang, Y. Zhao, X. Zhang, X. Yang, Y. Chen, Z. Chu, Q. Ye, X. Li, Z. Yin and J. You, *Nat. Photonics*, 2019, **13**, 460; (e) Y. Lv, R. Yuan, B. Cai, B. Bahrami, A. H. Chowdhury, C. Yang, Y. Wu, Q. Qiao, S. Liu and W.-H. Zhang, *Angew. Chem., Int. Ed.*, 2020, **59**, 11969; (f) X. Xu, H. Zhang, E. Li, P. Ru, H. Chen, Z. Chen, Y. Wu, H. Tian and W.-H. Zhu, *Chem. Sci.*, 2020, **11**, 3132.

2 (a) NREL Chart, <https://www.nrel.gov/pv/assets/pdfs/best-research-cell-efficiencies.20200925.pdf>; (b) G. Kim, H. Min, K. S. Lee, D. Y. Lee, S. M. Yoon and S. I. Seok, *Science*, 2020, **370**, 108.

3 (a) E. H. Jung, N. J. Jeon, E. Y. Park, C. S. Moon, T. J. Shin, T.-Y. Yang, J. H. Noh and J. Seo, *Nature*, 2019, **567**, 511; (b) H. Min, M. Kim, S.-U. Lee, H. Kim, G. Kim, K. Choi, J. H. Lee and S. I. Seok, *Science*, 2019, **366**, 749.

4 S.-H. Turren-Cruz, A. Hagfeldt and M. Saliba, *Science*, 2018, **362**, 449.

5 J.-W. Lee, D.-H. Kim, H.-S. Kim, S.-W. Seo, S. M. Cho and N.-G. Park, *Adv. Energy Mater.*, 2015, **5**, 1501310.

6 J.-W. Lee, S. Tan, T.-H. Han, R. Wang, L. Zhang, C. Park, M. Yoon, C. Choi, M. Xu, M. E. Liao, S.-J. Lee, S. Nuryyeva, C. Zhu, K. Huynh, M. S. Goorsky, Y. Huang, X. Pan and Y. Yang, *Nat. Commun.*, 2020, **11**, 5514.

7 W. Rehman, D. P. McMeekin, J. B. Patel, R. L. Milot, M. B. Johnston, H. J. Snaith and L. M. Herz, *Energy Environ. Sci.*, 2017, **10**, 361.

8 Y. Chen, Z. Yang, X. Jia, Y. Wu, N. Yuan, J. Ding, W.-H. Zhang and S. Liu, *Nano Energy*, 2019, **61**, 148.

9 (a) Y. Chen, J. Yang, S. Wang, Y. Wu, N. Yuan and W.-H. Zhang, *iScience*, 2020, **23**, 100762; (b) J. Yang, Y. Chen, W. Tang, S. Wang, Q. Ma, Y. Wu, N. Yuan, J. Ding and W.-H. Zhang, *J. Energy Chem.*, 2020, **48**, 217; (c) Q. Yao, Q. Xue, Z. Li, K. Zhang, T. Zhang, N. Li, S. Yang, C. J. Brabec, H.-L. Yip and Y. Cao, *Adv. Mater.*, 2020, **32**, 2000571.

10 Y. Wu, P. Wang, S. Wang, Z. Wang, B. Cai, X. Zheng, Y. Chen, N. Yuan, J. Ding and W.-H. Zhang, *ChemSusChem*, 2018, **11**, 837.

11 D. Yang, R. Yang, K. Wang, C. Wu, X. Zhu, J. Feng, X. Ren, G. Fang, S. Priya and S. Liu, *Nat. Commun.*, 2018, **9**, 3239.

12 X. Zheng, B. Chen, J. Dai, Y. Fang, Y. Bai, Y. Lin, H. Wei, X. C. Zeng and J. Huang, *Nat. Energy*, 2017, **2**, 17102.

13 (a) N. Li, S. Tao, Y. Chen, X. Niu, C. K. Onwudinanti, C. Hu, Z. Qiu, Z. Xu, G. Zheng, L. Wang, Y. Zhang, L. Li, H. Liu, Y. Lun, J. Hong, X. Wang, Y. Liu, H. Xie, Y. Gao, Y. Bai, S. Yang, G. Brocks, Q. Chen and H. Zhou, *Nat. Energy*, 2019, **4**, 408; (b) J. M. Ball and A. Petrozza, *Nat. Energy*, 2016, **1**, 16149.

14 Z. Li, M. Yang, J.-S. Park, S.-H. Wei, J. J. Berry and K. Zhu, *Chem. Mater.*, 2016, **28**, 284.

15 (a) D.-Y. Son, J.-W. Lee, Y. J. Choi, I.-H. Jang, S. Lee, P. J. Yoo, H. Shin, N. Ahn, M. Choi, D. Kim and N.-G. Park, *Nat. Energy*, 2016, **1**, 16081; (b) W. S. Yang, B.-W. Park, E. H. Jung, N. J. Jeon, Y. C. Kim, D. U. Lee, S. S. Shin, J. Seo, E. K. Kim, J. H. Noh and S. I. Seok, *Science*, 2017, **356**, 1376.

16 (a) X. Zheng, Y. Deng, B. Chen, H. Wei, X. Xiao, Y. Fang, Y. Lin, Z. Yu, Y. Liu, Q. Wang and J. Huang, *Adv. Mater.*, 2018, **30**, 1803428; (b) R. Wang, J. Xue, K.-L. Wang, Z.-K. Wang, Y. Luo, D. Fenning, G. Xu, S. Nuryyeva, T. Huang, Y. Zhao, J. L. Yang, J. Zhu, M. Wang, S. Tan, I. Yavuz, K. N. Houk and Y. Yang, *Science*, 2019, **366**, 1509.

17 C. A. McAuliffe and S. G. Murray, *Inorg. Chim. Acta*, 1972, **6**, 103.

18 Y. Chen, Z. Yang, S. Wang, X. Zheng, Y. Wu, N. Yuan, W.-H. Zhang and S. Liu, *Adv. Mater.*, 2018, **30**, 1805660.

19 M. Bieri and T. Bürgi, *Langmuir*, 2006, **22**, 8379.

20 P. R. Palaniappan, N. Krishnakumar and M. Vadivelu, *Aquat. Sci.*, 2008, **70**, 314.

21 N. Ahn, D. Y. Son, I. H. Jang, S. M. Kang, M. Choi and N. G. Park, *J. Am. Chem. Soc.*, 2015, **137**, 8696.

22 N. S. Sisombath, F. Jalilehvand, A. C. Schell and Q. Wu, *Inorg. Chem.*, 2014, **53**, 12459.

23 L. Wang, H. Zhou, J. Hu, B. Huang, M. Sun, B. Dong, G. Zheng, Y. Huang, Y. Chen, L. Li, Z. Xu, N. Li, Z. Liu, Q. Chen, L.-D. Sun and C.-H. Yan, *Science*, 2019, **363**, 265.

24 H. Zhao, Y. Han, Z. Xu, C. Duan, S. Yang, S. Yuan, Z. Yang, Z. Liu and S. Liu, *Adv. Energy Mater.*, 2019, **9**, 1902279.

25 D. Xin, S. Tie, R. Yuan, X. Zheng, J. Zhu and W.-H. Zhang, *ACS Appl. Mater. Interfaces*, 2019, **11**, 44233.

26 J. Wang, W. Li and W.-J. Yin, *Adv. Mater.*, 2020, **32**, 1906115.

27 Z. Xu, Z. Liu, N. Li, G. Tang, G. Zheng, C. Zhu, Y. Chen, L. Wang, Y. Huang, L. Li, N. Zhou, J. Hong, Q. Chen and H. Zhou, *Adv. Mater.*, 2019, **31**, 1900390.

28 (a) S. De Wolf, J. Holovsky, S.-J. Moon, P. Löper, B. Niesen, M. Ledinsky, F.-J. Haug, J.-H. Yum and C. Ballif, *J. Phys. Chem. Lett.*, 2014, **5**, 1035; (b) M. Ledinsky, T. Schönfeldová, J. Holovský, E. Aydin, Z. Hájková, L. Landová, N. Neyková, A. Fejfar and S. De Wolf, *J. Phys. Chem. Lett.*, 2019, **10**, 1368.

29 D. P. McMeekin, G. Sadoughi, W. Rehman, G. E. Eperon, M. Saliba, M. T. Horantner, A. Haghhighirad, N. Sakai, L. Korte, B. Rech, M. B. Johnston, L. M. Herz and H. J. Snaith, *Science*, 2016, **351**, 151.

30 J. W. Lee, H. S. Kim and N. G. Park, *Acc. Chem. Res.*, 2016, **49**, 311.

31 S. Li, K. Fan, Y. Cui, S. Leng, Y. Ying, W. Zou, Z. Liu, C.-Z. Li, K. Yao and H. Huang, *ACS Energy Lett.*, 2020, **5**, 2015.

32 J. Liu, Y. Yao, S. Xiao and X. Gu, *J. Phys. D: Appl. Phys.*, 2018, **51**, 123001.

33 R. H. Bube, *J. Appl. Phys.*, 1962, **33**, 1733.

34 G.-J. A. H. Wetzelaer, M. Scheepers, A. M. Sempere, C. Momblona, J. Ávila and H. J. Bolink, *Adv. Mater.*, 2015, **27**, 1837.

35 C. L. Davies, M. R. Filip, J. B. Patel, T. W. Crothers, C. Verdi, A. D. Wright, R. L. Milot, F. Giustino, M. B. Johnston and L. M. Herz, *Nat. Commun.*, 2018, **9**, 293.

36 M. Bernechea, N. C. Miller, G. Xercavins, D. So, A. Stavrinidis and G. Konstantatos, *Nat. Photonics*, 2016, **10**, 521.

37 D. Yang, X. Zhou, R. Yang, Z. Yang, W. Yu, X. Wang, C. Li, S. Liu and R. P. H. Chang, *Energy Environ. Sci.*, 2016, **9**, 3071.



38 (a) Y. Fan, J. Fang, X. Chang, M.-C. Tang, D. Barrit, Z. Xu, Z. Jiang, J. Wen, H. Zhao, T. Niu, D.-M. Smilgies, S. Jin, Z. Liu, E. Q. Li, A. Amassian, S. Liu and K. Zhao, *Joule*, 2019, **3**, 2485; (b) H. Tsai, R. Asadpour, J.-C. Blancon, C. C. Stoumpos, O. Durand, J. W. Strzalka, B. Chen, R. Verduzco, P. M. Ajayan, S. Tretiak, J. Even, M. A. Alam, M. G. Kanatzidis, W. Nie and A. D. Mohite, *Science*, 2018, **360**, 67.

39 (a) H. Tan, F. Che, M. Wei, Y. Zhao, M. I. Saidaminov, P. Todorović, D. Broberg, G. Walters, F. Tan, T. Zhuang, B. Sun, Z. Liang, H. Yuan, E. Fron, J. Kim, Z. Yang, O. Voznyy, M. Asta and E. H. Sargent, *Nat. Commun.*, 2018, **9**, 3100; (b) Y. Chen, W. Tang, Y. Wu, R. Yuan, J. Yang, W. Shan, S. Zhang and W.-H. Zhang, *Sol. RRL*, 2020, **4**, 2000344.

40 A. S. Brown and M. A. Green, *Prog. Photovoltaics*, 2002, **10**, 299.

41 W. Tang, Y. Chen, J. Yang, R. Yuan, Y. Lv, Q. Ma, Y. Wu, P. Zhang and W.-H. Zhang, *J. Power Sources*, 2021, **482**, 228965.

